# Nano-tailoring the Surface Structure for the Monolithic High-Performance Antireflection Polymer Film

By *Kiwoon Choi, Sung Ho Park, Young Min Song, Yong Tak Lee, Chang Kwon Hwangbo, Hoichang Yang,* and *Han Sup Lee**

Both single-layer and multilayer antireflection (AR) coatings between a bulk substrate and air have been used extensively to reduce surface reflection. These coating methods utilize the destructive interference between the lights reflected from the interfaces to minimize the total intensity of the reflected light.[1,2] However, the AR characteristics obtained with the coating methods can only be observed for a limited wavelength range and for an incidence angle close to the normal incidence. These drawbacks of the conventional coating methods can be sufficiently overcome either by the graded refractive index (RI) layers method or by the antireflective structure (ARS) method.[3,4]

The graded RI layers method and ARS method utilize optical impedance matching at two interfaces at air and substrate by making the RI of the AR layer vary gradually from the RI of air($n_o$) to that of the substrate($n_{sub}$) along the normal direction. In contrast with the coating methods, the graded RI layers method and ARS method were theoretically predicted to show broadband AR behavior of up to one order of magnitude and omnidirectional AR for an incidence angle of up to 80 degrees.[3]

Generally, two main approaches have been adopted to ensure that the RI changes gradually from $n_o$ to $n_{sub}$. One approach is to apply multiple layers with various RI values;[4–6] the other approach is to fabricate an ARS of a continuously tapered morphology similar to the morphology of the corneal nipple array of a moth eye.[7–11]

Surface reflection can reportedly be significantly reduced by the successive application of five layers of $SiO_2$ and $TiO_2$ with refractive indices between 1.05 and 2.05 on an AlN (n = 2.05) substrate via oblique-angle deposition with an electron beam evaporation method.[6] This possibility demonstrates how the well-controlled graded RI profile of the multiple layers can enhance the AR behavior.

Over the past decade, researchers have also focused on the use of a sub-wavelength ARS with a tapered morphology as a more practical method for ultrabroadband and omnidirectional AR[8,9] and these works have been well reviewed.[10,11] The way various ARSs, such as paraboloids (circular), cones, and Gaussian bell shapes, affect the AR has been evaluated previously.[12,13] Even though the quantitative reflectance from the surface is sensitively affected not only by the ARS shape but by the exact dimensions of the ARS, the paraboloid, which ensures the linear RI change in the AR layers, has been shown to be one of the best ARSs in terms of its relatively low surface reflectance.[13]

Various inorganic optical components have been replaced with the plastic materials due to their good mechanical and optical properties, easy and fast processibility, and their lightness. Polymethylmethacrylate (PMMA) has been extensively used as a transparent polymer for various optics and optoelectronics applications. Here, we present a method to nano-tailor the shape and dimensions of the ARS on the poly(methyl methacrylate) (PMMA) surface and the effect of nano-shaping on the AR performance has been characterized.

To find the optimum dimensions of ARS, we first calculate the reflectance theoretically from an ARS surface using a three-dimensional rigorous coupled-wave analysis (RCWA) method.[14] We set the spacing between adjacent paraboloids to 100 nm which is small enough to prevent Mie and Rayleigh scattering with the wavelengths used and convenient for experimental purposes.[15,16] Because minimum spacing must exist between two adjacent paraboloids, the diameter of the paraboloid base is set to 85 nm, which is almost the maximum attainable experimentally for a lattice spacing of 100 nm[17] and sixfold hexagonal symmetry of ARSs are modeled. **Figure 1a** shows the calculated reflectance from one surface with hexagonally packed ARSs of various heights.[18] As expected, the flat surface (height = 0) shows a reflectance (R) of approximately 3.9%. Lower reflectance is generally predicted for the greater height of a paraboloid with a fixed base diameter. However, the slight and slow fluctuation of the reflectance with the height can be also observed. The average reflectance is calculated and plotted in Figure 1b as a function of the paraboloid height. The results in Figure 1b indicate that as the paraboloid height increases the average reflectance decreases fast initially and reaches a minimum at about 210 nm.

To fabricate ARS of proposed dimensions for the optimum AR performance experimentally, we have to carefully consider

[*] K. Choi, S. H. Park, Prof. H. Yang, Prof. H. S. Lee
Department of Advanced Fiber Engineering
Inha University
253 Young-hyun-dong
Nam-gu, Incheon, 402–751 (Republic of Korea)
E-mail: hslee@inha.ac.kr
Prof. C. K. Hwangbo
Department of Physics
Inha University
253 Young-hyun-dong
Nam-gu, Incheon, 402–751 (Republic of Korea)
Y. M. Song, Prof. Y. T. Lee
Department of Information and Communications
Gwangju Institute of Science and Technology
1 Oryong-dong, Buk-gu, Gwangju, 500–712 (Republic of Korea)

DOI: 10.1002/adma.201001678

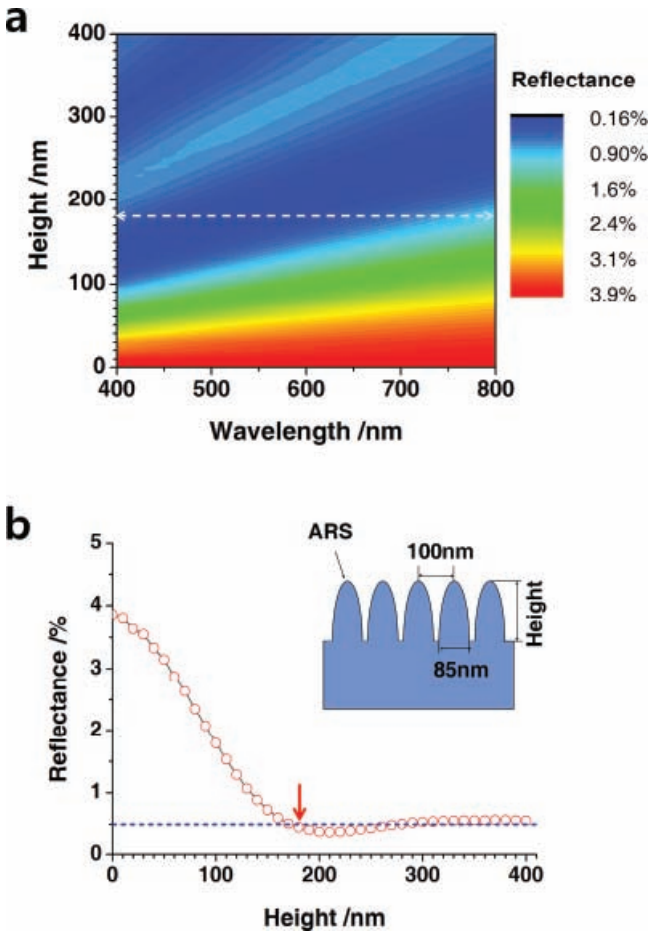


**Figure 1.** Calculated reflectance from one surface with paraboloids in hexagonal packing. a, Reflectance over a wavelength range of 400 nm to 800 nm. b, Average reflectance as a function of paraboloid height. The white line in a corresponds to the position indicated by the arrow in b. Reflectance of 0.5% is highlighted with the blue line in b. The inset of b shows a schematic cross-sectional image.

the effect of the ARS height on the mechanical stability. If the aspect ratio (L/D; length/base diameter of paraboloid) of the ARS increases above a certain critical value, a number of ARSs may locally adhere to each other to form bundles. Local adhesion has been observed at 3.0 aspect ratio, and for an even higher aspect ratio, even larger bundles have been formed.[19] (See Figure S1.) Since the reflectance value less than 0.5% has been predicted for an ARS height between about 180 nm and 270 nm, 180 nm ARS height appears to be an appropriate dimension for ensuring the low reflectance while maintaining the capability of the ARSs to stand straight on the surface.

To fabricate the ARSs experimentally on a PMMA surface, we prepared a well-ordered anodized aluminum oxide (AAO) template with the double anodization process through which hexagonally packed cylindrical pores are to be formed.[20,21] (see Supporting Information for details) By controlling the process parameters of time and temperature during anodization and chemical etching, we can control the dimensions of the cylindrical pores, such as the depth and diameter of the pores. First, as shown in Figure S2, we established the general relation between the pore dimensions and control parameters during the anodization and chemical etching processes. The data confirm the linear relation between the depth and diameter of the pores and the time of the anodization and etching, respectively. Nevertheless, we need to carefully modify the cylindrical pore shapes to the parabolic ARS shape as predicted in Figure 1.

It is possible to nano-tailor the shape and dimensions of the pores in the aluminum template by applying the multistep anodization and etching method,[22,23] the schematic process of which is illustrated in **Figure 2a**. As shown in Figure 2a, the 3-step anodization and etching method will produce eventually 3-level pores consisting of first-level, second-level, and third-level. First, the initial diameter and depth of the pores in the first level are formed during the first step anodization and etching processes. When the second step anodization and etching processes are applied, the initial diameter and depth of the pores in the second level are formed and the pore diameter in the first level is increased according to the relation described in Figure S2. The continuation of this process enables the nanotailoring of the shape and dimension of the pores in the aluminum template. Figure 2b compares the theoretical parabolic shape and the experimentally simulated shape (5-level pore) obtained from the 5-step anodization and etching processes.[24] (Figure S3 shows the RI profiles of the interface layer in the AR film with ideal paraboloids as well as the five experimental models.) Note that the overall pore depth (L) and eventual diameter (D) of the pores in the first level are determined by the total anodization time (T) and the total etching time (t), respectively. For the given L and D, the precise shape of the pore can be controlled by a careful distribution of the $T_i$ and $t_i$ in each step. Table S1 lists the $T_i$ and $t_i$ values used to fabricate the multilevel pores in the aluminum oxide template.

The top and side view images of the AAO templates fabricated with the 1-step, 3-step, and 5-step anodization and etching processes are shown in Figure 2c and 2d. The data in those two figure confirm the hexagonally packed multilevel pores have a narrow distribution of the pore diameter and depth. The fact that the sharp edges between the two adjacent levels in Figure 2b were subjected to a faster etching rate helps produce the gradually tapered morphology of the pores and eliminates any discontinuous change in dimensions between the two adjacent levels. We can therefore observe in the last image in Figure 2d that the contour of the pores obtained with the 5-step anodization and etching processes closely resembles the shape given in Figure 2b. Note also, as indicated by the arrow in Figure 2c, that the six intersections of a hexagonal pore are slightly elevated (by about 10 nm to 20 nm) from the common base plate.[17]

Pores in AAO can be filled with the molten polymer by mean of the vacuum-assisted surface wetting method.[19,25–27] This method makes use of the surface tension difference between the aluminum oxide wall and the molten polymer and the pressure difference between the inside (vacuum state) and outside (atmospheric state) of the pores. (For more details, refer to the Figure S4 in the Supporting information) After the polymers in the pores are cooled, the AAO template can be separated from the polymer either chemically[25,26] or mechanically.[19,23]

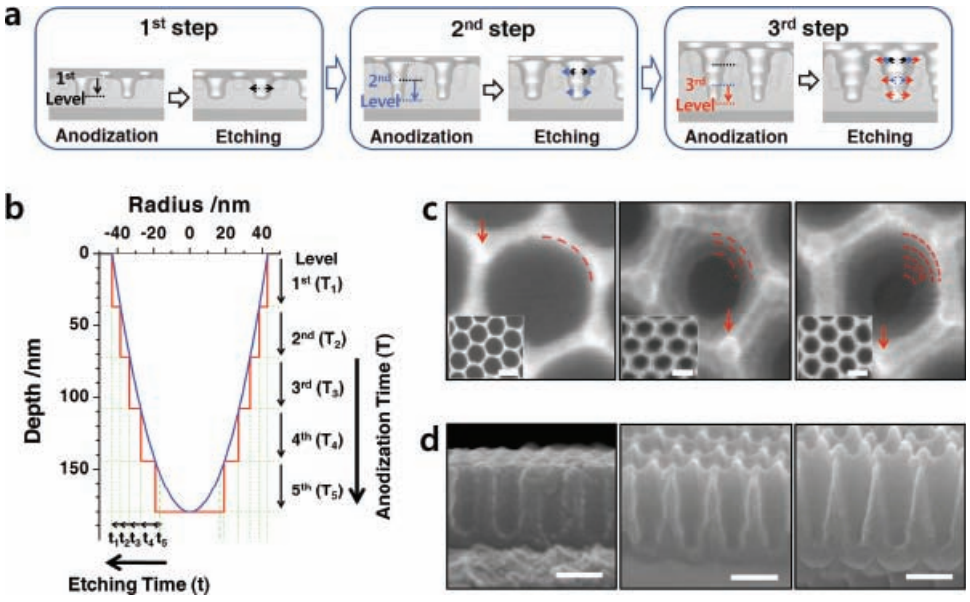


**Figure 2.** Multistep anodization and etching process for the fabrication of AAO with multi-level pores. a, 3-step anodization and etching processes for producing 3-level pores of a given morphology. b, Cross-sectional shape of an ideal paraboloid (in blue line) and experimentally simulated pore shape (in red line) obtainable from the 5-step anodization and etching processes. c, Top view of pores in AAO obtained from a 1-step (left), 3-step (middle), and 5-step (right) anodization and etching processes. The insets demonstrate regular packing of pores. The demarcations between steps are indicated by the dotted red line. The elevated spot at the intersections in the hexagon is indicated by a red arrow. d, Side view of pores in AAO obtained from the 1-step (left), 3-step (middle), and 5-step (right) anodization and etching processes. The scale bars in c and d correspond to 100 nm.

The top view of the resultant polymer film confirms the presence of hexagonally packed monolithic ARS structures on the PMMA substrate (**Figure 3a**). Careful inspection of the enlarged image in Figure 3a reveals that the intersections of the hexagonal shapes have darker spots, which are related to the elevated spots at the intersections in Figure 2c. Figure 3b and 3c show side and oblique SEM images of the 1-level, 3-level, and 5-level ARSs. As the number of anodization and etching steps increases, the shape of the ARS turns into a tapered morphology because the diameter is continually reduced from the base (first level) to the tip (last level) of the ARS. The ARS has a height of 180 nm ± 10 nm and a base diameter of 85 nm ± 2 nm. We also

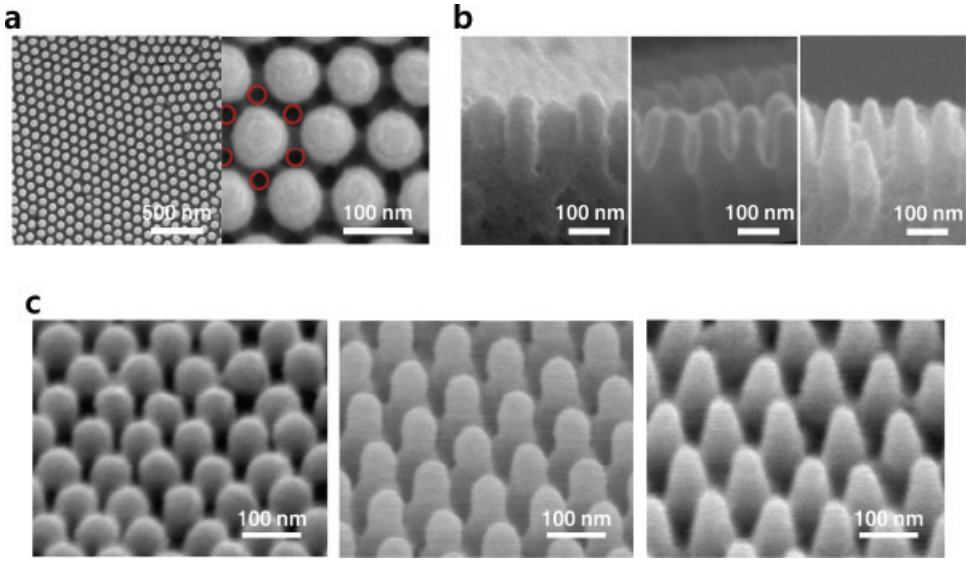


**Figure 3.** ARSs on the surface. a, Top view of a 2-level sample. All five samples show similar top views, confirming the hexagonal packing of the ARSs. The depressed regions at the intersections of a hexagon can be confirmed from the darker spots and few are denoted with red circles. b and c, Side and oblique views of ARSs obtained through the 1-step (left), 3-step (middle), and 5-step (right) anodization and etching processes, respectively.

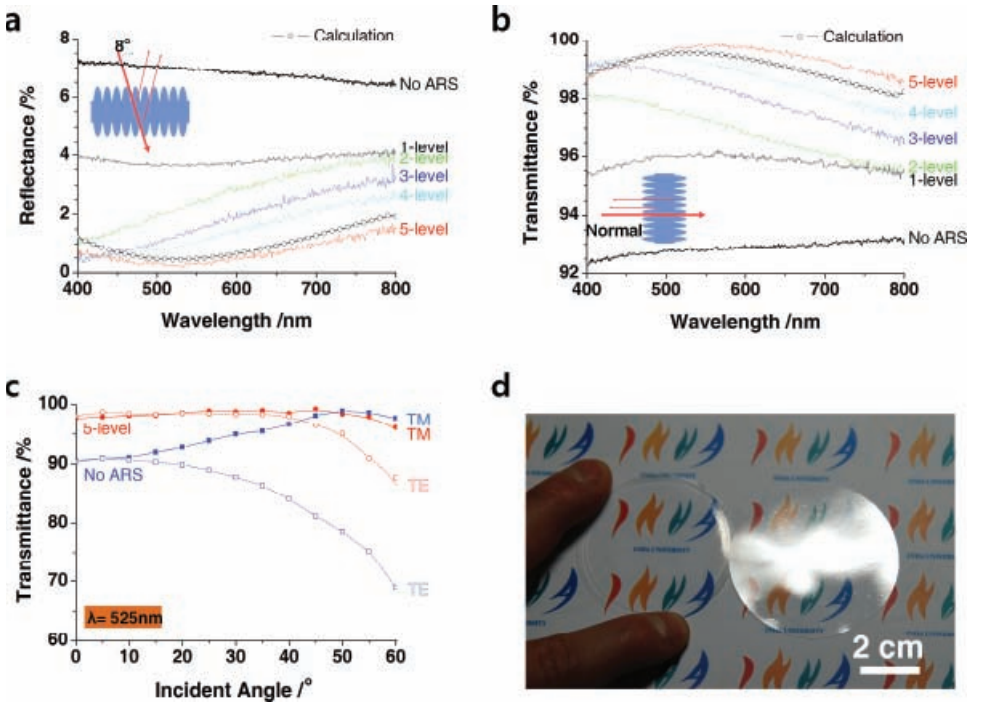


**Figure 4.** Reflectance and transmittance. a and b, Measured and calculated total reflectance (a) and transmittance values (b). The reflectance and transmittance values from AR films with ARSs obtained from the 1-step to 5-step anodization and etching processes are shown. The calculation was done for the film with paraboloids (85 nm base diameter, 180 nm height) in hexagonal packing on both surfaces of 100 μm thick film. The incidence angles for the reflectance and transmittance measurements are 8 degrees and 0 degrees, respectively. The measurement error of each data point in a and b is approximately 0.1%. c, The transmittance of TE and TM polarized lights of 525 nm wavelength through the reference film and 5-step film as a function of the incidence angle. d, Digital images of the 5-step film (left) and the reference film (right). The data in a and b were obtained with an integrating sphere and the data in c were obtained without an integrating sphere.

found that an aspect ratio of about 2.1 is low enough to ensure that most of paraboloid ARSs stand up straight on the substrate surface for this material.

To verify the effect of the nano-tailoring the shape and dimensions of ARS on the AR performance experimentally, we measured the total reflectance (with 8 degrees incidence angle) and transmittance (normal incidence) with the AR films made (**Figure 4a** and 4b). The results obtained with flat film (without any ARS) are also included. As expected from the theoretical prediction (of about 3.9% for one surface), the reflectance from both flat surfaces is somewhere between 7.0% and 7.5% for a wavelength range of 400 nm to 800 nm (Figure 4a). The overall reflectance of the ARS film is gradually lowered as the number of anodization and etching step increases. The 5-level ARS film has an average reflectance of 0.64% at a wavelength range of 400 nm to 800 nm, and a reflectance of less than 1% is observed for all wavelengths in the 400 nm to 710 nm range. The minimum reflectance of 0.15% is measured at 532 nm. To the best of our knowledge, the 5-level ARS film fabricated in this work has the best AR performance ever reported for transparent polymer AR films. This demonstrates that the nano-tailoring the shape and dimensions of the surface ARS can be useful method to fabricate the polymer AR film with the optimum performance.

The theoretically predicted values for AR film with paraboloid ARS of proposed dimensions (a height of 180 nm and a diameter of 85 nm) are included in Figure 4a and 4b.[14] Note that there is close similarity between the calculated and experimental values for the 5-level AR film. The experimental reflectance from the 5-level ARS film is slightly better than the theoretically calculated reflectance. The discrepancy appears to be related to the elevated spots at the hexagonal intersections and the overall macroscopic (microscale) non-flatness of the AAO template, which contributes to the gradual change of the RI, especially at the interface of the substrate and the base of the paraboloids (as indicated by the arrow in Figure 2c).

The transmittance data also support the reflectance results (Figure 4b). The film with the 5-level ARSs has an average transmittance of 99.4% at a wavelength range of 400 nm to 800 nm. A transmittance value higher than 99% was observed for all wavelengths in the 420 nm to 740 nm range, and the maximum transmittance was 99.9% for a 565 nm wavelength. Again the experimental values from the 5-level AR film resemble the theoretical values for the paraboloid ARS with a corresponding height and base diameter. For most wavelengths above 470 nm, the experimental transmittance values are even better than the theoretical values, probably due to the reasons mentioned above. Below this wavelength, the strong absorption characteristics of PMMA seem to affect the experimental transmittance. (Our calculation ignores the non-negligible absorption of PMMA at wavelengths near 400 nm.)

The transmittance was also measured as a function of the incidence angle for two polarizations (TM and TE) at 525 nm

with 5-level ARS films and flat films (Figure 4c). Compared with the flat reference film, the 5-level films show greater improvement in the AR performance for incidence angles away from normal illumination ($\theta$ = 0 degree). This behavior might be extremely useful for applications of AR film that require high transmittance at various incidence angles, such as solar cells and flat panel display units.[8,28–30]

The reflectance difference between the 5-level ARS film and the flat PMMA film is demonstrated visually in Figure 4d. The film on the left-hand side is the 5-level ARS film and the film on the right-hand side is the flat film. The non-flatness of the film can be inferred from the localized strong surface reflection from the flat film. However, no noticeable surface reflection can be observed with the 5-level ARS film. The right side edge of the 5-level ARS film has strong surface reflection because the outside rim (of about 2 mm to 3 mm) has no ARSs on the surface. With careful inspection of the AR film shown on the left-hand side of Figure 4d, the region with ARSs can be distinguished from the region without ARSs.

These results highlight the potential of fabricating a high-performance AR film by forming nano-tailored structures on polymer films. We have demonstrated that the shape and dimensions of a surface nanostructure can be finely controlled by applying a multistep anodization process to an aluminum disk. We have also shown that the shape of the nanopores in the AAO template can be transferred with exactitude to the polymer surface if the pores are filled with molten polymer by means of a vacuum-assisted surface wetting method. The experimental reflectance and transmittance observed with the 5-level ARS films in this work have the best AR performance ever reported for transparent polymer films. Furthermore, the close resemblance between the experimental values with the 5-level ARS films and the theoretical values appears to indicate that the best experimental AR values in this work might be close to the extreme limit of any experimental approaches for a system that is similar to the one used in this work. Because the AR film fabricated in this work is monolithic, it shows none of the usual problems associated with most multilayer AR coating methods: namely, the problems of material selection, thermal mismatches, and the instability of thin film stack.[31] The AAO template used in this work might be unsuitable for the mass production of ARSs on a film surface. However, various replication methods widely used these days may be utilized to make a flexible, robust template with an identical pore structure, and those methods might lead to a solution for industrial fabrication of AR films.[19,32–34]

## *Experimental Section*

*Optical modeling and simulation*: To calculate the reflectance from the AR films, we used a three-dimensional rigorous coupled-wave analysis (RCWA) method.[14] In the RCWA calculation, parabola-shaped structures with sixfold hexagonal symmetry were modeled. The radius of the ARSs has a paraboloid tapered profile in a radial direction.[12,13] The fifth diffraction order is used to calculate the diffraction efficiency, which is a sufficient number to stabilize the results numerically. We considered the dispersion of PMMA to obtain the exact result at each wavelength.[34] For the calculation of the transmittance and reflectance of the PMMA film with ARSs on both surfaces, the substrate thickness was fixed at 100 μm. The calculated values at each wavelength were averaged to remove the rapid fluctuations caused by interference of the light reflected at the top and bottom surfaces. Absorption by the PMMA film was not considered during the simulation.

*Optical measurements*: The reflectance and transmittance values in Figure 4a and 4b were measured with a spectrophotometer (Perkin Elmer lambda 650) equipped with an integrating sphere for a wavelength range of 400 nm to 800 nm at an interval of 1 nm. Deuterium and tungsten lamps were the light sources. The absolute reflectance was obtained from the ratio of the sample spectrum and the reference spectrum. The reference spectrum was obtained with aluminum-sputtered glass, which was calibrated with a standard mirror (OMT Solution). The reported reflectance and transmittance are the average values of several data obtained from various spots of identical sample. The transmittance values at the different incidence angles shown in Figure 4c were obtained without an integrating sphere.

## Supporting Information

Supporting information is available online from Wiley InterScience or from the author.

## Acknowledgements

We thank Prof. Jinsub Choi of Inha University for developing and assisting with the anodization process. This work was supported by the 2009 Project for the Technique Innovation in the Knowledge Economy, which was sponsored by the Ministry of Knowledge Economy, the City of Incheon, and Inha University in the Republic of Korea. C. K. Hwangbo was supported in part by the Korea Science and Engineering Foundation (KOSEF) grant funded by the Ministry of Education, Science and Technology in the Republic of Korea. (Quantum Photonic Science Research Center)

Received: May 7, 2010
Published online: July 12, 2010

[1] S. Walheim, E. Schäffer, J. Mlynek, U. Steiner, *Science* **1999**, *283*, 520.
[2] H. A. Macleod, *Thin- film optical filters*, *2nd ed.*, Adam Hilger Ltd., Bristol, U.K., **1986**.
[3] D. Poitras, J. A. Dobrowolski, *Appl. Opt.* **2004**, *43*, 1286.
[4] S. Chhajed, M. F. Schubert, J. K. Kim, E. F. Schubert, *Appl. Phys. Lett.* **2008**, *93*, 251108.
[5] S. R. Kennedy, M. J. Brett, *Appl. Opt.* **2003**, *42*, 4573.
[6] J.-Q. Xi, M. F. Schubert, J. K. Kim, E. F. Schubert, M. Chen, S.-Y. Lin, W. Liu, J. A. Smart, *Nat. Photon.* **2007**, *1*, 176.
[7] P. B. Clapham, M. C. Hutley, *Nature* **1973**, *244*, 281.
[8] Y. J. Lee, D. S. Ruby, D. W. Peters, B. B. McKenzie, J. W. P. Hsu, *Nano Lett.* **2008**, *6*, 1501.
[9] S. L. Diedenhofen, G. Vecchi, R. E. Algra, A. Hartsuiker, O. L. Muskens, G. Immink, E. P. A. M. Bakkers, W. L. Vos, J. G. Rivas, *Adv. Mater.* **2009**, *21*, 973.
[10] S. J. Randolph, J. D. Fowlkes, P. D. Rack, *Crit. Rev. Solid State Mater. Sci.* **2006**, *31*, 55.
[11] Y. Li, J. Zhang, B. Yang, *Nano Today* **2010**, *5*, 117.
[12] D. G. Stavenga, S. Foletti, G. Palasantzas, K. Arikawa, *Proc. R. Soc. B* **2006**, *273*, 661.
[13] H. M. Wu, C. M. Lai, L. H. Peng, *Appl. Phys. Lett.* **2008**, *93*, 211903.
[14] M. G. Moharam, T. K. Gayload, *J. Opt. Soc. Am.* **1981**, *71*, 811.

[15] W. H. Southwell, *J. Opt. Soc. Am. A* **1991**, *8*, 549.
[16] A. P. Li, F. Müller, A. Birner, K. Nielsch, U. Gösele, *J. Appl. Phys.* **1998**, *84*, 6023.
[17] Z. L. Xiao, C. Y. Han, U. Welp, H. H. Wang, W. K. Kwok, G. A. Willing, J. M. Hiller, R. E. Cook, D. J. Miller, G. W. Crabtree, *Nano Lett.* **2002**, *2*, 1293.
[18] S. A. Boden, D. M. Bagnall, *Appl. Phys. Lett.* **2008**, *93*, 133108.
[19] S. Grimm, R. Giesa, K. Sklarek, A. Langner, U. Gösele, H.-W. Schmidt, M. Steinhart, *Nano Lett.* **2008**, *8*, 1954.
[20] H. Masuda, K. Fukuda, *Science* **1995**, *268*, 1466.
[21] J. Choi, R. B. Wehrspohn, U. Gösele, *Adv. Mater.* **2003**, *15*, 1531.
[22] T. Nagaura, F. Takeuchi, S. Inoue, *Electrochim. Acta.* **2009**, *53*, 2109.
[23] T. Yanagishita, K. Yasui, T. Kondo, Y. Kawamoto, K. Nishio, H. Masuda, *Chem. Lett.* **2007**, *36*, 530.
[24] P. Lalanne, D. Lemercier-Lalanne, *J. Mod. Opt.* **1996**, *43*, 2063.
[25] M. Steinhart, J. H. Wendorff, A. Greiner, R. B. Wehrspohn, K. Nielsch, J. Schilling, J. Choi, U. Gösele, *Science* **2002**, *296*, 1997.
[26] M. Zhang, P. Dobriyal, J. T. Chen, T. P. Russell, *Nano Lett.* **2006**, *6*, 1075.
[27] R. Kwak, H. E. Jeong, K. Y. Suh, *Small* **2009**, *5*, 790.
[28] Y. M. Song, E. S. Choi, J. S. Yu, Y. T. Lee, *Opt. Express* **2009**, *17*, 20991.
[29] J. Zhu, C.-M. Hsu, Z. Yu, S. Fan, Y. Cui, *Nano Lett.* **2010**, DOI: 10.1021/nl9034237.
[30] Y. Li, F. Li, J. Zhang, C. Wang, S. Zhu, H. Yu, *Appl. Phys. Lett.* **2010**, *96*, 153305.
[31] U. Schulz, *Appl. Opt.* **2006**, *45*, 1608.
[32] Q. Chen, G. Hubbard, P. A. Shields, C. Liu, D. W. E. Allsopp, W. N. Wang, S. Abbott, *Appl. Phys. Lett.* **2009**, *94*, 263118.
[33] E. Kim, Y. Xia, M. Whitesides, *Nature* **1995**, *376*, 581.
[34] S. N. Kasarova, N. G. Sultanova, C. D. Ivanov, I. D. Nikolov, *Opt. Mater.* **2007**, *29*, 1481.